中北大学学报(自然科学版)
JOURNAL OF NORTH UNIVERSITY OF CHINA(NATURAL SCIENCE EDITION)
2026年 第47卷 第3期(总第227期)
Vol. 47 No. 3 2026(Sum No. 227)

文章编号：1673-3193(2026)03-0306-09 J. North Univ. China, Nat. Sci. Ed., 2026, 47(3): 306-314.

噻二唑功能化的紫精在中性水性有机液流电池中的性能研究

张智超[1]，闫绪杰[2]，李秀林[3]，杨云峰[1*]

(1. 中北大学 化学与化工学院，山西 太原 030051；2. 华盛顿大学 工程学院，华盛顿 西雅图 98105；
3. 中国科学院煤炭化学研究所 煤炭高效低碳利用全国重点实验室，山西 太原 030001)

摘　要：中性水系有机氧化还原流电池(AORFBs)因其活性物质来源广泛、分子结构可精准调控及环境友好等优势，被视为可扩展储能与可再生能源发电的关键储能技术之一。然而，现有的有机氧化还原活性分子仍面临多重性能瓶颈，包括溶解度偏低、氧化还原电位偏离水溶液热力学稳定窗口，以及在长期循环过程中容量衰减显著，严重制约了其在中性水系电解质体系中的工程化应用。本文设计并合成了一类新型噻二唑中间体的吡啶鎓衍生物4,4′-(1,3,4-噻二唑-2,5-二基)双(1-(3-三甲基铵基)丙基)吡啶-1-鎓(BnSn)和4,4′-(1,3,-噻二唑-2,5-二基)双(1-甲基吡啶-1-鎓)(BnSm)，通过在分子骨架中引入1,3,4-噻二唑桥联单元，系统拓展了共轭体系，并协同构建了基于氮原子孤对电子的分子间氢键网络。该分子在纯水中的溶解度达0.89 mol·L^{-1}，呈现高度可逆的双电子行为，其主还原峰电位为−0.98 V，且在中性缓冲电解液中展现出优异的电化学稳定性。作为负极活性物质，其能提供卓越的长期稳定性。在0.05 mol·L^{-1}和600 A·m^{-2}电流密度的条件下，500次恒电流充放电循环后容量保持率高于70%，对应平均单圈衰减率仅为0.016%，每天衰减率为0.16%。综合密度泛函理论模拟与机理研究结果表明：1,3,4-噻二唑桥不仅可以通过增强分子内电子离域提升氧化还原中心的结构刚性与热力学稳定性，还借助其强极性与氢键供受体双功能特性，有效抑制了活性物种的不可逆二聚、水解及自由基介导的降解路径，从而同步优化了溶解动力学、电荷转移效率与循环耐久性。

关键词：能源储存；液流电池；水系有机液流电池；氧化还原物种；分子间氢键

中图分类号：TM911 **文献标识码：**A **doi:** 10.62756/jnuc.issn.1673-3193.2026.03.0021

引用格式：张智超，闫绪杰，李秀林，等. 噻二唑功能化的紫精在中性水性有机液流电池中的性能研究[J]. 中北大学学报(自然科学版)，2026，47(3)：306-314.

ZHANG Zhichao, YAN Xujie, LI Xiulin, et al. Study on performance of thiadiazole-functionalized viologen derivatives in neutral aqueous organic flow batteries[J]. Journal of North University of China(Natural Science Edition), 2026, 47(3): 306-314.

Study on Performance of Thiadiazole-Functionalized Viologen Derivatives in Neutral Aqueous Organic Flow Batteries

ZHANG Zhichao[1], YAN Xujie[2], LI Xiulin[3], YANG Yunfeng[1*]

(1. School of Chemistry and Chemical Engineering, North University of China, Taiyuan 030051, China;
2. College of Engineeing, University of Washington, Seattle 98105, USA;
3. State Key Laboratory of Coal Conversion, Institute of Coal Chemistry, Chinese Academy of Sciences, Taiyuan 030001, China)

收稿日期：2026-03-31
基金项目：山西省自然科学基金(202502060302014，202303021221256)
作者简介：张智超(1999—)，男，硕士生，主要从事中性水系有机液流电池阳极电解质方向的研究。
* **通信作者：**杨云峰(1970—)，男，教授，博士，从事有机合成、高分子材料制备及性能研究。E-mail：yangyunfeng@nuc.edu.cn。

Abstract: Neutral aqueous organic redox flow batteries (AORFBs) represent a compelling candidate for scalable energy storage integrated with renewable power generation, largely due to the earth-abundant, tunable, and sustainable nature of organic electroactive compounds. However, current redox-active species still face critical limitations, including insufficient solubility, inadequate voltage window compatibility, and poor cycling stability, hindering their practical deployment in neutral-pH aqueous electrolytes. In this work, a new class of pyridinium derivatives of thiadiazole intermediates, namely 4,4′-(1,3,4-thiadiazole-2,5-diyl)bis(1-(3-trimethylammonio)propyl)pyridin-1-ium (BnSn) and 4,4′-(1,3,4-thiadiazole-2,5-diyl)bis(1-methylpyridin-1-ium) (BnSm) were designed and synthesized. By introducing a 1,3,4-thiadiazole bridging unit into the molecular framework, the conjugation system was systematically extended, and an intermolecular hydrogen-bonding network based on nitrogen lone pair electrons was synergistically constructed. The resulting molecule achieves exceptional aqueous solubility (0.89 mol·L^{-1}), a well-positioned low potential (−0.98 V), and outstanding electrochemical reversibility under neutral conditions. When employed as the negative electrolyte, it delivers remarkable long-term stability. After 500 constant-current charge-discharge cycles at 0.05 mol·L^{-1} and a current density of 600 A·m^{-2}, the capacity retention rate remained above 70%, corresponding to an average cycle decay rate of only 0.016% and a daily decay rate of 0.16%. Combined density functional theory calculations and experimental mechanistic analysis indicate that the 1,3,4-thiadiazole bridge not only enhances the intramolecular electron delocalization to improve the structural rigidity and thermodynamic stability of the redox center, but also effectively inhibits the irreversible dimerization, hydrolysis and free radical-mediated degradation pathways of active species by virtue of its strong polarity and hydrogen bond donor-acceptor dual functional properties. Thus, it simultaneously optimizes the dissolution kinetics, charge transfer efficiency and cycle durability.

Key words: energy storage; flow battery; aqueous organic flow battery; redox species; intermolecular hydrogen bonding

0 Introduction

Global energy systems still depend on fossil fuels, harming the environment. The development of clean energy is becoming increasingly important. Solar and wind power are intermittent, complicating grid integration[1-3]. Aqueous redox flow batteries (ARFBs) enable scalable, safe energy storage through reversible redox reactions. Inorganic ARFBs face challenges from scarce metals, ion crossover and hydrogen evolution[4-10]; while aqueous organic redox flow batteries (AORFBs) instead use abundant, tunable organic molecules. Their electrochemical properties can be tailored for low-cost, large-scale deployment. This advantage is especially important in neutral-pH systems, where it boosts durability and sustainability. The key organic candidates include quinones[11-12], nitroxide[13-14], phenazines[15-16] and viologens[17-19]. Multi-pyridyl viologens perform well as anolytes, but lack cycling stability for real applications. In contrast, the π-conjugated bridges have improved stability and kinetics.

Recent studies have shown that the bridging units can improve conjugation in organic redox molecules, boosting their performance in AORFBs. We proposed a diazole-based bridges at strategic sites in the viologen core to enhance stability, reversibility and solubility. Unlike carbon-only aromatic bridges, which are limited to π—π conjugation, diazole bridges support both p—π and π—π conjugation and form intermolecular hydrogen bonds. This dual action extends conjugation during redox cycling, suppressing degradation and improving electrochemical performance. Here, we introduced a thiadiazole bridge to boost viologen solubility in water. Two ammonium-functionalized viologens 4,4′-(1,3,4-thiadiazole-2,5-diyl)bis(1-(3-trimethylammonio)propyl)pyridin-1-ium (BnSn) and 4,4′-(1,3,4-thiadiazole-2,5-diyl)bis(1-methylpyridin-1-ium) (BnSm) with this bridge

were designed and synthesized. The thiadiazole unit increases hydrophilicity and drives strong intermolecular hydrogen bonding, enhancing both solubility and stability. Its nitrogen lone pairs extend conjugation in the reduced state and narrow HOMO-SOMO and HOMO-LUMO gaps, improving redox reversibility. In a neutral BnSn||FeNCl cell, >95% capacity is retained after 500 cycles (0.023% fade per cycle). *In-situ* spectroscopy confirms stable structure and solvent H-bonding during cycling, revealing the mechanism.

1 Preparation of electrolyte and the assembly of battery

1.1 Synthesis of electrolytes

All the reagents used in this paper are from Shanghai Energy Chemical, of analytical grade, and do not require further purification. The synthesis routes of BnSn and BnSm are shown in Fig. 1.

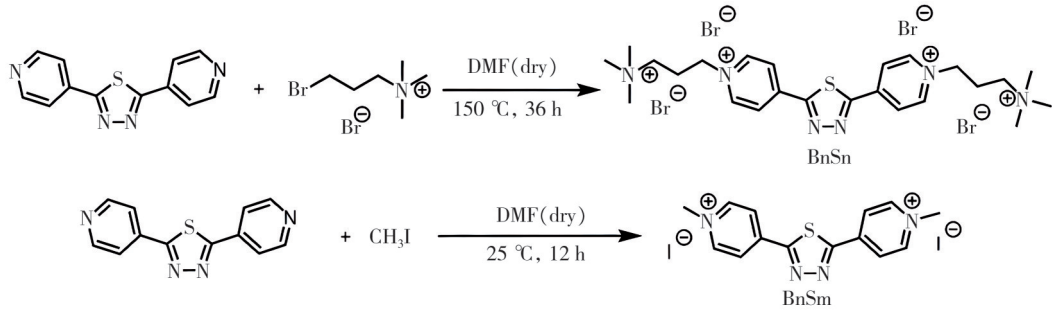

Fig. 1 Synthesis routes of BnSn and BnSm

Synthesis of BnSn: 2,5-di(4-Pyridyl)-1,3,4-thiadiazole (BnS) (3.6 g, 15 mmol) and (3-bromopropyl) trimethylammonium bromide (12.5 g, 40 mmol) were dissolved in anhydrous DMF (80 mL) in a 250 mL three-necked flask under N_2. The mixture was refluxed at 150 ℃ for 36 h, then cooled to room temperature. The crude product was isolated by filtration and washed sequentially with DMF, anhydrous acetonitrile, and diethyl ether until the filtrate became colorless. After drying under vacuum, the product was obtained in 80% yield (8.7 g). ^{1}H NMR (400 MHz, D_2O) δ 9.10 (d, J=7.1 Hz, 4H), 8.71 (d, J=7.0 Hz, 4H), 4.76 (t, J=7.8 Hz, 4H), 3.54~3.46 (m, 4H), 3.10 (s, 18H), 2.67~2.53 (m, 4H).

Synthesis of BnSm: BnS (3.6 g, 15 mmol) was dissolved in anhydrous DMF (80 mL) in a 250 mL three-necked flask under N_2, and methyl iodide (100 mL) was added. The mixture was stirred at room temperature for 12 h. The precipitate was collected by filtration and washed sequentially with DMF, anhydrous acetonitrile, and diethyl ether until the filtrate became colourless. The crude product was dissolved in minimal water to near saturation, then acetonitrile was slowly added to induce precipitation. After filtration and drying under vacuum, a pale red solid was obtained in 80% yield (5.6 g). ^{1}H NMR (400 MHz, DMSO-d_6): δ 9.23 (d, J=6.8 Hz, 4H), 8.82 (d, J=6.9 Hz, 4H), 4.45 (s, 6H).

Synthesis of FcNCl: FcNCl was synthesized according to reported method. Ferrocenylmethyl dimethylamine (8.2 ml, 40 mmol), methyl chloride (120 mL, 120 mmol) and 40 mL dry CH_3CN were added to a round-bottom flask, which was stirred at room temperature overnight. The product was collected by filtration, washed with 10 mL ether for 3 times, and dried under vacuum. A yellow solid was obtained in 95% yield (11.21 g). ^{1}H NMR (400 MHz, D_2O) δ 4.44 (s, 2H), 4.36 (s, H), 4.32 (s, 2H), 4.21 (s, 5H), 2.88 (s, 9H).

1.2 Battery assembly

The cell assembly consisted of two bakelite endplates, a graphite current collector plate, and graphite felt electrodes, separated by an anion-exchange membrane (Fumasep FAA-3-50). The geometric active area is 4 cm^2. Prior to use, deionized water was sparged with high-purity N_2 for 30 min and sonicated to remove dissolved oxygen. The anolyte contained BnSm or BnSn (0.5 mol·L^{-1}), the

catholyte contained FcNCl（1.0 mol·L^{-1}），and both compartments employed 1.0 mol·L^{-1} NaCl as supporting electrolyte. Electrolytes were circulated at 60 mL·min^{-1}. Before sealing，the cell was purged with N_2 three times to eliminate residual O_2. All full-cell tests were performed under galvanostatic cycling at a current density of 600 A·m^{-2} within a voltage window of 0.1～1.5 V. Notably，elevated electrolyte concentration exacerbated water crossover，particularly when anolyte and catholyte concentrations were matched. To mitigate this，the catholyte concentration was reduced，and controlled water addition was applied to the anolyte during extended cycling.

1.3　Electrolyte configuration

For neutral aqueous organic redox flow batteries（AORFBs），the anolyte and catholyte concentrations were held constant at 0.05 mol·L^{-1} and 0.1 mol·L^{-1} for low-concentration configurations（8 mL anolyte/10 mL catholyte），and at 0.50 mol·L^{-1} for high-concentration configurations（5 mL anolyte/25 mL catholyte），using BnSn or BnSm as anolyte active species and FcNCl as catholyte active species.

1.4　Density functional theory（DFT） calculation

All calculations were performed using Gaussian 16. Geometry optimizations and frequency analyses used B3LYP-D3（BJ）/6-311+G（d，p），with solvation modeled *via* the SMD continuum model. Optimized structures were confirmed as minima by absence of imaginary frequencies；thermal corrections to Gibbs free energy were obtained from the same frequency calculations. Single-point energies were computed at the same level. Default convergence criteria were applied（max force＜4.5×10^{-4} Hartree/Bohr；RMS force＜3.0×10^{-4} Hartree/Bohr）.

2　Result and analysis

2.1　Screening of redox-active molecules

DFT[20] was employed to elucidate how molecular structure governs electronic and redox behavior. Fig. 2（a）displays the computed HOMO and LUMO energies for viologens bearing distinct linkers. Across all derivatives，the spatial distribution of these frontier orbitals remains remarkably uniform.

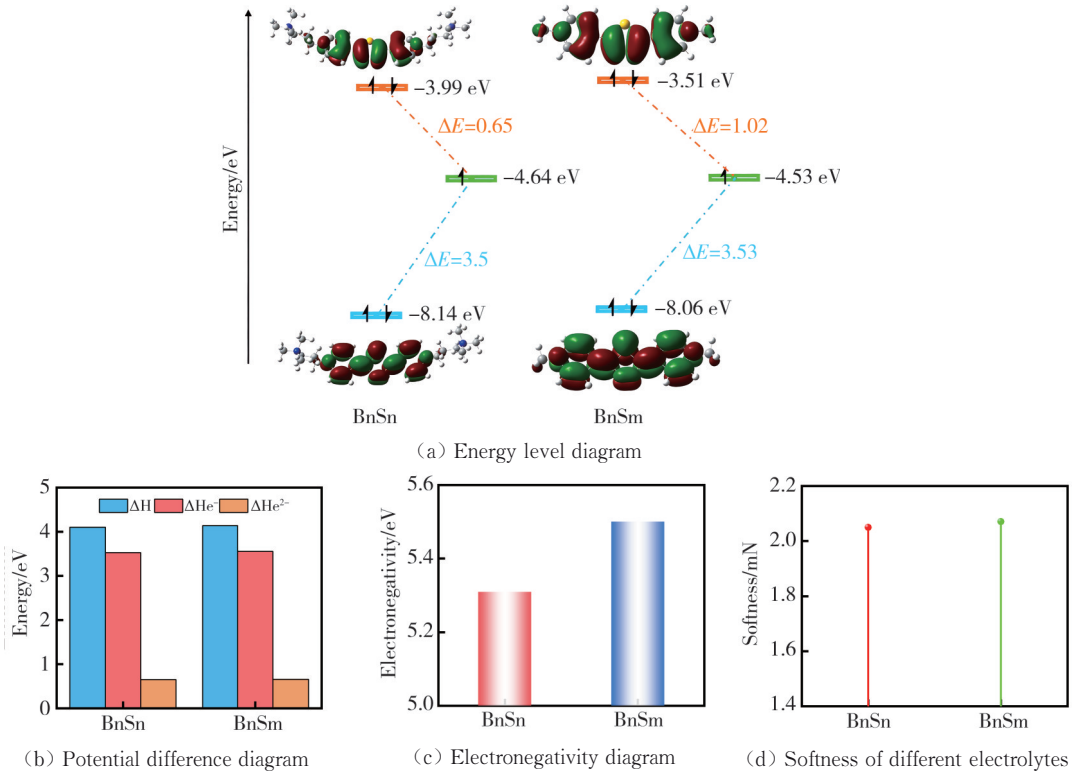

（a）Energy level diagram

（b）Potential difference diagram　（c）Electronegativity diagram　（d）Softness of different electrolytes

Fig. 2　Energy level diagrams and chemical descriptor diagrams of different electrolytes

Notably, BnSn displays a marked anodic shift in its first redox potential (ΔE_{2e}) relative to BnSm, while the second redox gap (ΔE_{1e}) is nearly identical. Fig. 2(b) indicates that a reduced overall ΔE generally correlates with enhanced charge transport, superior redox reversibility and diminished kinetic barriers. Further computational analysis in Fig. 2(c) indicates that the thiadiazole bridge in BnSn imparts higher atomic electronegativity compared to the linker in BnSm. Furthermore, as shown in Fig. 2(d), BnSn displays the smallest global softness parameter among the series, suggesting reduced intermolecular association and greater conformational flexibility, both of which contribute to improved electrochemical reversibility. Importantly, both diazole-linked BnSn and BnSm were synthesized in gram-scale quantities using a streamlined, one-pot procedure. This scalable, cost-efficient route significantly advances the practical deployment of neutral aqueous organic redox flow batteries.

The schematic diagram of the battery is shown in Fig. 3(a). Additionally, by combining with comprehensive cyclic voltammetry (CV) data, the electrochemical behaviors of BnSn and BnSm can be clearly differentiate. The CV analyses in Fig. 3(b) and Fig. 3(c) reveal that the redox potentials of the two viologen derivatives are −0.98 V and −0.78 V (vs. Ag/AgCl), respectively. These potential shifts arise predominantly from differences in the electron-donating strength of the linker substituents. A linear correlation between peak current and the square root of scan rate as shown in Fig. 3(d) and Fig. 3(e). From the solvation free energy diagram in Fig. 3(f), it can be clearly seen that the solubility of BnSn is higher than that of other electrolytes. Notably, BnSn achieves a significantly higher aqueous solubility (0.89 mol·L^{-1}) than BnSm.

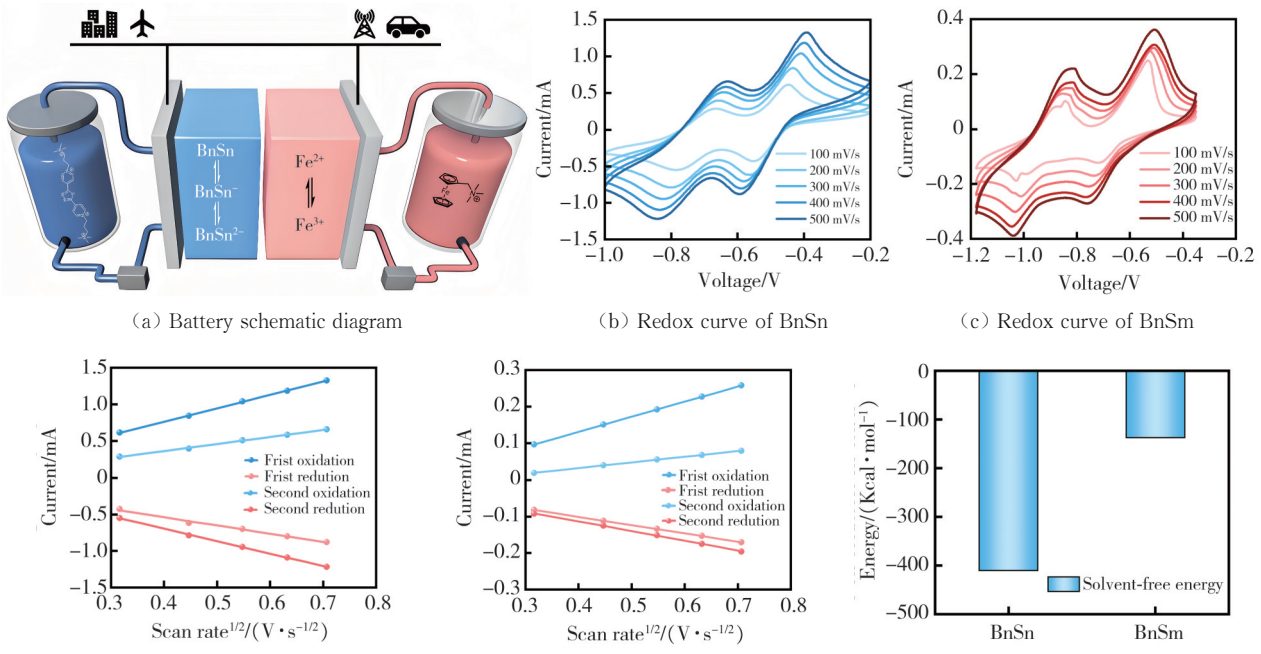

(a) Battery schematic diagram (b) Redox curve of BnSn (c) Redox curve of BnSm

(d) BnSn peak current versus scan rate (e) BnSm peak current versus scan rate (f) Solvent-free energy diagram

Fig. 3 Electrochemical performance comparison between BnSn and BnSm

2.2 Electrochemical performance evaluation of redox flow batteries

Fig. 4 depicts the molecular packing and spatial organization of BnSn and BnSm within the neutral AORFB architecture. Notably, when FeNCl serves as the supporting electrolyte, the BnSm-based cell delivers a substantially higher open-circuit voltage than its BnSn counterpart. As shown in Fig. 4(a), while the BnSn-FeNCl pairing delivers an open-circuit voltage (OCV) of 1.20 V, the BnSm-FeNCl configuration yields a slightly lower OCV of 1.34 V. Rate capability of AORFBs employing 0.05 mol·L^{-1} BnSn electrolyte was systematically assessed using

Fumasep FAA-3-50 membranes. Additionally, from Fig. 4(b), upon increasing the current density from 200 A·m^{-2} (19.3 mAh) to 1 000 A·m^{-2} (2.9 mAh), the cell retains 15% of its initial discharge capacity. Moreover, at a current density of 1 000 A·m^{-2}, the energy efficiency (EE) of BnSn still remains at 60%. At full state-of-charge in Fig. 4(c), the BnSn system achieves a peak power density of 1 580 W·m^{-2}, surpassing most reported viologen-based systems. In parallel, in Fig. 4 (d), the 0.05 mol·L^{-1} BnSm||FeNCl cell underwent galvanostatic cycling for 500 cycles, showing only a modest capacity decay, averaging 0.25% per cycle. Fig. 4(e) shows that the BnSn-based neutral AORFB retained 70% of its starting capacity after 500 cycles, corresponding to an ultra-low degradation rate of 0.016% per cycle. These findings demonstrate that integrating a hydrogen-bond-capable molecular scaffold into the viologen backbone significantly improves structural resilience during repeated redox cycling, thereby suppressing capacity loss induced by state-of-charge variations and enhancing overall operational longevity.

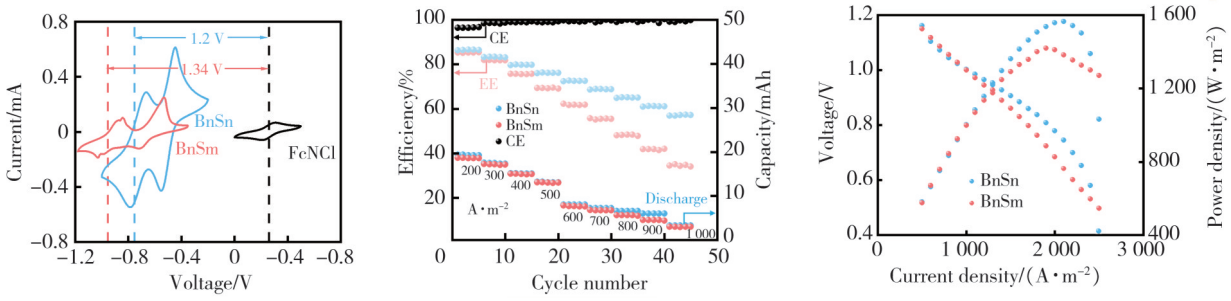

(a) OCV curves of BnSn and BnSm　(b) CE, EE and discharge of BnSn and BnSm　(c) Power density diagram

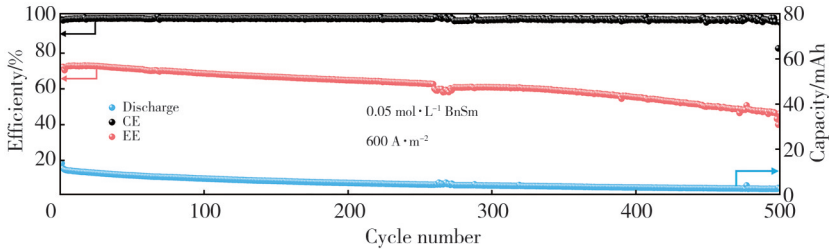

(d) Cyclic performance graph of BnSm

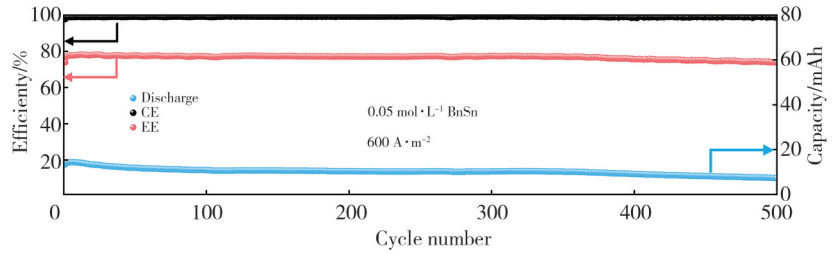

(e) Cyclic performance graph of BnSn

Fig. 4　Comparison of the cycling stability of BnSm and BnSn in low-concentration AORFBs

To assess real-world feasibility, the BnSn||FeNCl cell was evaluated under industrially relevant conditions using a 0.5 mol·L^{-1} concentration. As shown in Fig. 5(a), the coulombic efficiency (CE) values of BnSm and BnSn can basically remain at 100%, but the energy efficiency (EE) and discharge capacity of BnSm are both lower than those of BnSn under the same current density. And at 800 A·m^{-2} current density, the EE of BnSn still reaches 65%. It can also be seen from Fig. 5(b) that the capacity decreases as the current density increases. Moreover, in Fig. 5(c), the time-current curve indicates the stable existence of the battery system. Concurrently, Fig. 5(d) shows that the 0.5 mol·L^{-1} BnSm||FeNCl cell demonstrates exceptional cycling stability over 200 galvanostatic cycles, with an average capacity fade of just 0.62% per cycle. Fig. 5(e) shows that the BnSn-

based neutral AORFB retained 65% of its initial capacity after the same number of cycles, with an extremely low degradation rate of only 0.086% per cycle.

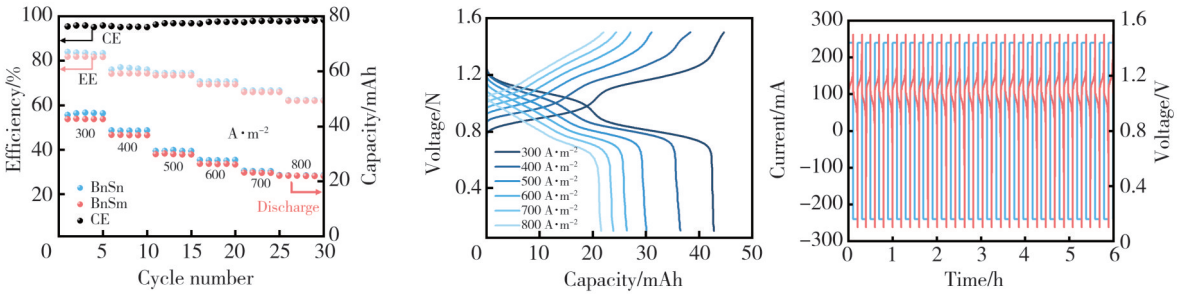

(a) CE, EE and discharge of BnSn and BnSm (b) Capacity-voltage curve (c) Time-current curve

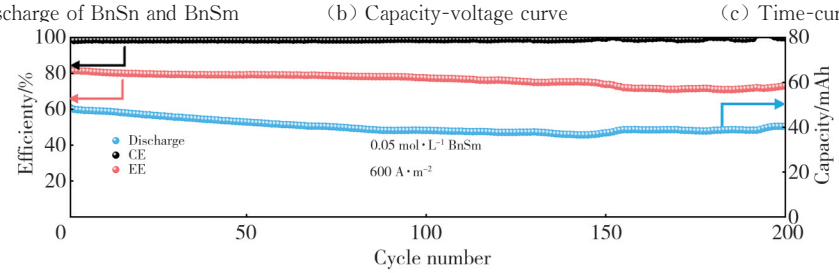

(d) Cyclic performance of BnSm

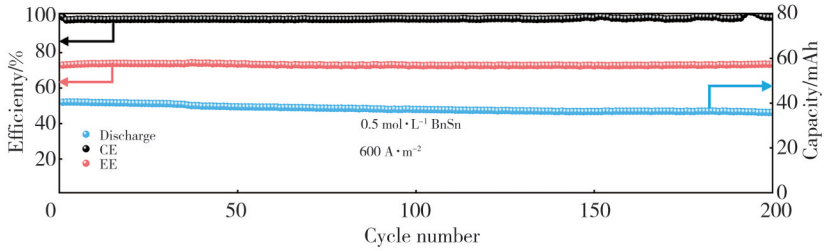

(e) Cyclic performance of BnSn

Fig. 5 Comparison of the cycling stability between BnSm and BnSn in high-concentration AORFBs

2.3 Investigation mechanisms

To elucidate the redox mechanism and potential degradation routes of BnSn during electrochemical cycling, a comprehensive operando characterization study was carried out on its negolyte solution. Electron paramagnetic resonance (EPR) spectra in Fig. 6(a) identifies a characteristic signal at g= 2.033 (351.4 mT), unambiguously assigned to the BnSn• radical anion. As charging proceeds, this signal intensifies monotonically and peaks at 50% state-of-charge, indicating progressive one-electron reduction and accumulation of the stable radical species. Complementary *in-situ* UV-Vis analysis in Fig. 6(b) captures real-time molecular transformations: upon oxidation, the absorption band centered at 308 nm steadily weakens, while a new feature grows at 445 nm, correlating directly with the visible color shift from pale off-white to deep brownish-black. During subsequent discharge, the spectral changes reverse completely, the 445 nm band fades and the 308 nm peak fully recover, demonstrating near-perfect spectral reversibility and confirming high-fidelity redox cycling without irreversible side reactions. Moreover, ^{1}H NMR titration experiments in Fig. 6(c) reveal a systematic upfield shift of the water proton resonance with increasing BnSn concentration, providing direct spectroscopic evidence for concentration-dependent hydrogen-bond network formation, specifically mediated by the thiadiazole-based linker, which acts as both H-bond acceptor and structural organizer within the molecular architecture.

Although the high-resolution mass spectrometry data acquired under operational conditions reveal trace signals consistent with minor side-chain hydrolysis,

slow decomposition, radical dimerization, and chloride-mediated nucleophilic substitution, the extent of such side reactions is minimal, no measurable impact on redox reversibility or long-term cycling integrity is observed. Integrating these findings with prior mechanistic insights, we proposed a coherent degradation pathway for BnSn, offering actionable design principles for next-generation viologen derivatives. As shown in Fig. 6(d), upon electrochemical reduction, BnSn sequentially accepts one and two electrons to generate the monoanionic ($BnSn^{\bullet}$) and dianionic ($BnSn^{2-}$) species, serving as the primary charge carriers. The α-carbon adjacent to the pyridinium ring, rendered highly electron-rich and nucleophilic in the reduced states, becomes susceptible to radical coupling, leading to formation of the C—C bonded dimer diBnSn. In the presence of chloride ions, this same electrophilic α-site undergoes nucleophilic substitution, yielding chlorinated dimers diBnSnCl. Concurrently, the structurally analogous BnSn undergoes parallel Cl^- attack at its α-position, affording BnSnCl. These parallel pathways highlight the critical role of substituent electronics and local steric environment in governing degradation selectivity. The comparison of power density, energy efficiency, current density and cost of reported viologen-based neutral AORFBs is shown in Tab. 1.

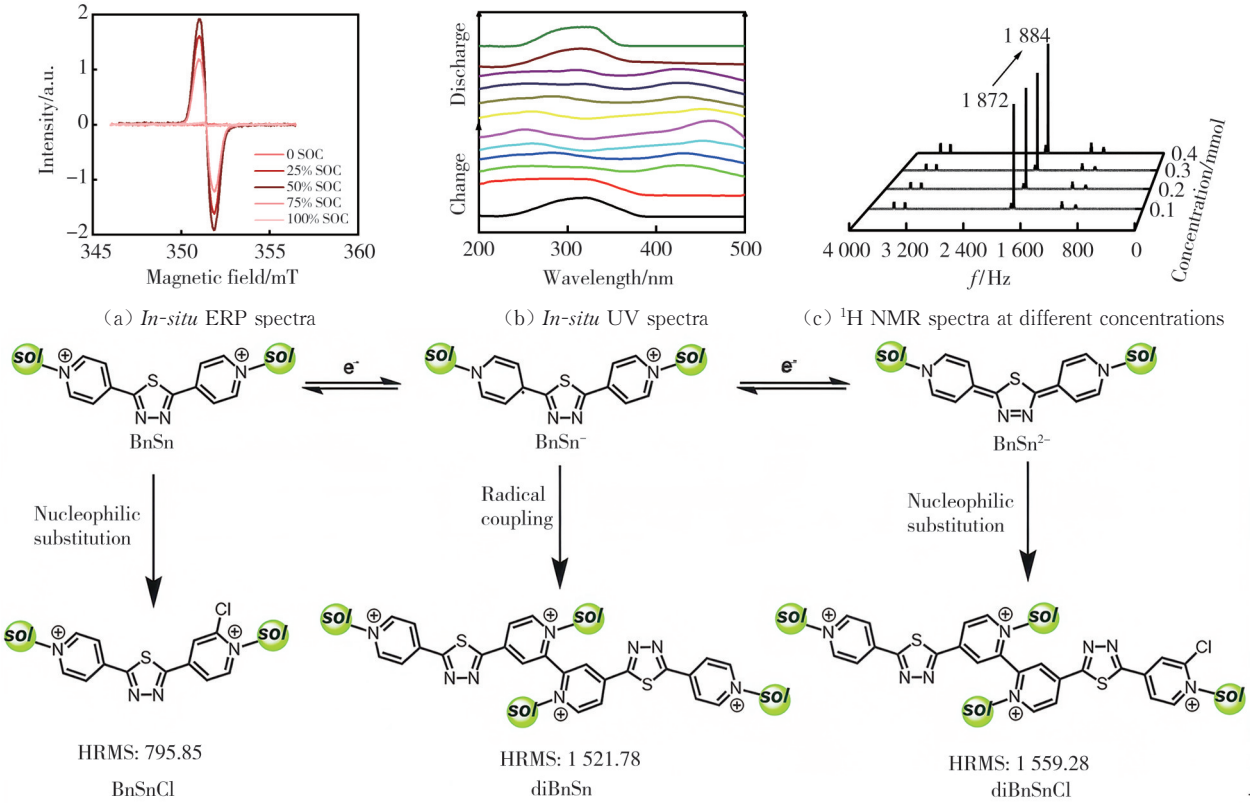

(a) *In-situ* ERP spectra　(b) *In-situ* UV spectra　(c) ^{1}H NMR spectra at different concentrations

(d) Redox behavior and degradation prediction

Fig. 6　Redox behavior and capacity degradation mechanism studies of BnSn

Tab. 1　Comparison of technical features of two-electron storage materials for neutral AORFBs

Anolyte	EE/%	Power density/(W•m^{-2})	Number of cycles	Current density/(A•m^{-2})	Cost/(¥•kg^{-1})
$(SPr)_2V$	58	920	300	600	7 836
$[(NPr)_2TV]Cl_4$	50	1 100	300	400	81 500
$[(Me)(NPr)V]Cl_3$	70	1 300	50	600	11 250
BnSn (this work)	**70**	**1 580**	**500**	**600**	**9 900**

3　Conclusion

In summary, we reported a practical synthetic method of water-soluble diazole-bridged viologens using a thiadiazole linker. The ammonium salts with strong intermolecular hydrogen bonding and

extended p—π/π—π conjugation. DFT shows the thiadiazole bridge enhances solubility *via* its electronegativity and H-bonding; the extended conjugation also shifts the redox potential negatively. In neutral BnSn||FeNCl AORFBs, we achieved higher operating voltage and robust cycling, with 0.016% capacity fade per cycle over 500 cycles, outperforming BnSm. *In-situ* characterization confirms the thiadiazole unit stabilizes the redox core by suppressing dimerization and degradation, while improving solubility and reversibility. This work advances neutral AORFBs for long-duration storage and offers general design principles for aqueous redox-active materials.

利益冲突声明/Conflict of Interests

所有作者声明不存在利益冲突。

All authors declare no relevant conflict of interests.

References:

[1] ISLAM S, WEERASINGHE H, et al. Diversifying the materials and technologies for the future of energy storage [J]. Energy & Fuels, 2025, 39(18): 8369-8390.

[2] ZUO P, YE C, JIAO Z, et al. Near-frictionless ion transport within triazine framework membranes [J]. Nature, 2023, 617(7960): 299-305.

[3] YAO Y, LEI J, SHI Y, et al. Assessment methods and performance metrics for redox flow batteries[J]. Nature Energy, 2021, 6(6): 582-588.

[4] LOPES P P, STAMENKOVIC V R. Past, present, and future of lead-acid batteries [J]. Science, 2020, 369 (6506): 923-924.

[5] BARBER D R. Apparent solar control of the effective capacity of a 110-V. 170 Ah lead-acid storage battery in an 11-year cycle [J]. Nature, 1962, 195 (4842): 684-687.

[6] ARMAND M, TARASCON J M. Building better batteries[J]. Nature, 2008, 451(7179): 652-657.

[7] SCHON T B, MCALLISTER B T, LI P F, et al. The rise of organic electrode materials for energy storage[J]. Chemical Society Reviews, 2016, 45(22): 6345-6404.

[8] ZHANG B, YANG X, HE B, et al. Thionated benzo [*c*] thiophen-1(3*H*)-one as an organic cathode with high capacity for sulfur-rich all organic lithium-ion batteries [J]. Journal of Materials Chemistry A, 2021, 9(25): 14444-14450.

[9] LI T, XING F, LIU T, et al. Cost, performance prediction and optimization of a vanadium flow battery by machine-learning[J]. Energy & Environmental Science, 2020, 13(11): 4353-4361.

[10] YUAN Z, YIN Y, XIE C, et al. Zinc-based flow batteries: advanced materials for zinc-based flow battery: development and challenge (adv. mater. 50/2019)[J]. Advanced Materials, 2019, 31(50): 1970356.

[11] ODOM S A. A less basic, basic organic flow battery[J]. Joule, 2018, 2(9): 1652-1653.

[12] SCHLEMMER W, NOTHDURFT P, PETZOLD A, et al. 2-methoxyhydroquinone from vanillin for aqueous redox-flow batteries[J]. Angewandte Chemie International Edition, 2020, 59(51): 22943-22946.

[13] FENG R, ZHANG X, MURUGESAN V, et al. Reversible ketone hydrogenation and dehydrogenation for aqueous organic redox flow batteries[J]. Science, 2021, 372(6544): 836-840.

[14] FENG R, CHEN Y, ZHANG X, et al. Proton-regulated alcohol oxidation for high-capacity ketone-based flow battery anolyte[J]. Joule, 2023, 7(7): 1609-1622.

[15] HOLLAS A, WEI X, MURUGESAN V, et al. A biomimetic high-capacity phenazine-based anolyte for aqueous organic redox flow batteries[J]. Nature Energy, 2018, 3(6): 508-514.

[16] PANG S, JIN S, YANG F, et al. A phenazine-based high-capacity and high-stability electrochemical CO_2 capture cell with coupled electricity storage[J], Nature Energy, 2023, 8: 1126-1136.

[17] ZHANG X, LIU X, ZHANG H, et al. Robust chalcogenophene viologens as anolytes for long-life aqueous organic redox flow batteries with high battery voltage[J]. ACS Applied Materials & Interfaces, 2022, 14(43): 48727-48733.

[18] LIU X, BAO C, WANG Z, et al. Meta-substituted thienoviologen with enhanced radical stability *via* π-π interaction modulation for neutral aqueous organic flow batteries [J]. Energy Storage Materials, 2024, 73: 103824.

[19] SULLIVAN P T, LIU H, LV X L, et al. Viologen hydrothermal synthesis and structure - property relationships for redox flow battery optimization [J]. Advanced Energy Materials, 2023, 13(34): 2203919.

[20] LU T. A comprehensive electron wavefunction analysis toolbox for chemists, multiwfn [J]. The Journal of Chemical Physics, 2024, 161(8): 082503.